

Phonon-driven intra-exciton Rabi oscillations in CsPbBr₃ halide perovskites

Received: 12 August 2022

Accepted: 10 February 2023

Published online: 24 February 2023

 Check for updates

Xuan Trung Nguyen¹, Katrin Winte¹, Daniel Timmer ¹, Yevgeny Rakita^{2,3}, Davide Raffaele Ceratti^{2,4,5}, Sigalit Aharon², Muhammad Sufyan Ramzan¹, Caterina Cocchi^{1,6}, Michael Lorke ⁷, Frank Jahnke ⁷, David Cahen ², Christoph Lienau ^{1,6,8} & Antonietta De Sio ^{1,6} ✉

Coupling electromagnetic radiation with matter, e.g., by resonant light fields in external optical cavities, is highly promising for tailoring the optoelectronic properties of functional materials on the nanoscale. Here, we demonstrate that even internal fields induced by coherent lattice motions can be used to control the transient excitonic optical response in CsPbBr₃ halide perovskite crystals. Upon resonant photoexcitation, two-dimensional electronic spectroscopy reveals an excitonic peak structure oscillating persistently with a 100-fs period for up to ~2 ps which does not match the frequency of any phonon modes of the crystals. Only at later times, beyond 2 ps, two low-frequency phonons of the lead-bromide lattice dominate the dynamics. We rationalize these findings by an unusual exciton-phonon coupling inducing off-resonant 100-fs Rabi oscillations between 1s and 2p excitons driven by the low-frequency phonons. As such, prevailing models for the electron-phonon coupling in halide perovskites are insufficient to explain these results. We propose the coupling of characteristic low-frequency phonon fields to intra-excitonic transitions in halide perovskites as the key to control the anharmonic response of these materials in order to establish new routes for enhancing their optoelectronic properties.

Coupling matter excitations, such as excitons, and localized electromagnetic radiation, e.g., via light modes in external optical or plasmonic resonators, may result in hybrid quasi-particles with both matter and field character¹. Excitons dressed by a light mode may profoundly alter the energy landscape of the material and its quantum dynamics^{1,2}. Such light-matter couplings are highly interesting for nanomaterial engineering, as they provide approaches for manipulating optoelectronic properties and photoinduced dynamics on the nanoscale, without modifying the material composition or crystal

structure^{3–9}. In the simplest view, the interaction of an exciton with a resonant quantized light mode is described by the Jaynes-Cummings model¹. The coupling strength $\hbar\Omega$ between the exciton and the field mode defines the energy oscillation rate between them. Strong coupling sets in when $\hbar\Omega$ exceeds the damping rates of both uncoupled systems. In optical spectra, it manifests itself as peak splittings or sidebands to a bare exciton resonance¹⁰, and, in the dynamics, as Rabi oscillations¹¹, a coherent, periodic energy exchange between matter and field.

¹Institut für Physik, Carl von Ossietzky Universität, 26129 Oldenburg, Germany. ²Department of Molecular Chemistry & Materials Science, Weizmann Institute of Science, 76100 Rehovot, Israel. ³Department of Materials Engineering, Ben-Gurion University of the Negev, 84105 Beer-Sheva, Israel. ⁴Institut Photo-voltaïque d'Île de France (IPVF), CNRS, Ecole Polytechnique, Palaiseau 91120, France. ⁵Sorbonne Université, CNRS, Collège de France, UMR 7574, Chimie de la Matière Condensée de Paris, Paris F-75005, France. ⁶Center for Nanoscale Dynamics (CeNaD), Carl von Ossietzky Universität, 26129 Oldenburg, Germany. ⁷Institut für Theoretische Physik, Universität Bremen, 28359 Bremen, Germany. ⁸Research Center Neurosensory Science, Carl von Ossietzky Universität, 26111 Oldenburg, Germany. ✉ e-mail: antonietta.de.sio@uni-oldenburg.de

Optical phonons in polar semiconductors are associated with electric fields confined inside the crystal and have a well-defined spectrum of allowed modes dictated by the specific crystal structure and material composition. The photoexcited charge density induces local displacements of the ions in the lattice generating a polarization field which can, in turn, interact with the charges. This leads to the formation of polaronic quasi-particles¹² with enhanced mass¹³ and reduced mobility¹² compared to free carriers. Usually, however, phonon fields are largely off-resonant with relevant electronic transitions. Hence, often, a single electronic state governs the interaction and the adiabatic treatment of polarons within the Born-Oppenheimer approximation is well justified. In contrast, strong light-matter coupling involves different electronic states.

There is increasing consensus that in halide perovskites (HaPs), the interaction of electronic excitations with the vibrational modes of the flexible polar lattice^{14–16} is crucial for their unique optoelectronic and transport properties^{17–19} that form the basis for their excellent device performance. Fundamental aspects of the underlying electron-phonon interactions in HaPs are, however, still debated. Established models developed for conventional semiconductors, such as the Fröhlich model²⁰ describing long-range electron-phonon interactions, have mostly been used to explain the observations of time-resolved spectroscopic studies^{14,21–25}. The Fröhlich model considers the lattice as a polarizable dielectric continuum and describes electron-phonon interactions by a coupling constant α which depends primarily on the values of the dielectric function in the high-frequency and static limit, on the charge density, and on a single phonon mode energy involved in the coupling^{12,20}. Results from time-dependent optical Kerr effect spectroscopy¹⁴, transient THz photoconductivity²², two-photon photoemission dynamics²⁶, and recent angle-resolved photoelectron spectroscopy experiments²⁵ have been interpreted based on the formation of large electron or hole polarons on sub-ps timescales. Signatures of phonon coherences^{23,24} after impulsive optical excitation in ultrafast experiments have been rationalized within dispersive excitation mechanisms, estimating electron-phonon couplings based on the Fröhlich model.

This model, however, neglects the real-space structure of the lattice and therefore cannot account for short-range interactions. Small polarons can be particularly important in low dimensional crystals, including two-dimensional HaPs²⁷, and they have also been suggested to form in bulk HaPs¹⁹. So far, experiments have mostly been interpreted using an adiabatic treatment of the electron-phonon coupling, whereas atomistic simulations^{28,29} indicate that nonadiabatic couplings may also play an important role, raising the question whether the underlying Born-Oppenheimer approximation indeed suffices to explain the optoelectronic properties of HaPs. Recent studies also suggest more complex scenarios including important contributions of dynamic lattice disorder³⁰ and anharmonicity^{17,31,32}.

Here, using ultrafast two-dimensional electronic spectroscopy (2DES), combined with model simulations of the nonlinear optical response, we report a clear breakdown of the adiabatic exciton-phonon coupling regime in CsPbBr₃ single crystals. Our data provide evidence for off-resonant Rabi oscillations between 1s and 2p excitons, driven by the characteristic low-frequency phonon modes of the lead-bromide lattice. This is in contrast with prevailing models for the electron-lattice interaction in HaPs. Our results suggest that the low-frequency phonon fields in the crystals can modulate the exciton population and thus may modify the transient optoelectronic properties of HaPs, analogous to strong light-matter couplings.

Results

Ultrafast two-dimensional electronic spectroscopy of CsPbBr₃ crystals

We investigate CsPbBr₃ single crystals in the orthorhombic phase at 20 K (Fig. 1a, upper panel). We perform 2DES measurements in a

partially collinear configuration in reflection³³ using a pair of phase-locked pump pulses, time-delayed by the coherence time τ , and a probe pulse, delayed by the waiting time T with respect to the second pump pulse (Fig. 1a lower panel).

For each T , we record differential reflectivity spectra as a function of τ and of the detection energy E_D . The real part of the Fourier transform (FT) of this time domain signal along τ provides energy-energy 2DES maps $A_{2D}(E_X, T, E_D)$, with E_X being the excitation energy (Methods). Since we study optically thick bulk crystals in reflection, the measured A_{2D} signal is dominated by the real part of the nonlinear optical susceptibility of the crystals^{33,34}, yielding dispersive lineshapes along E_D (Fig. 1b). The optical pulses allow for simultaneous resonant excitation of excitons and free carriers with an excess energy of ~200 meV in the continuum (Fig. S1). The 2DES data presented here have been recorded with a pump fluence of 4 $\mu\text{J}/\text{cm}^2$ ensuring low excitation densities below the Mott transition³³ and orders of magnitude below the photodamage limit³⁵.

The 2DES maps show a sharp dispersive diagonal peak at $E_0 = 2.345$ eV, and a dispersive vertically elongated cross-peak at higher E_X (Fig. 1b). The diagonal peak is commonly assigned³³ to 1s excitons with a binding energy of 40 meV³⁶. A vertically elongated cross-peak appears upon excitation and its shape remains essentially unchanged up to 12 ps (Fig. S2). Its amplitude decays slowly on timescales of ~2.5 ps and >50 ps (Fig. S3). This cross-peak arises from the optical excitation of free carriers in the sample. Coulomb interactions between free-carrier excitations and excitons may induce a slight broadening of the exciton resonance (excitation-induced dephasing, EID) or a resonance shift (excitation-induced shift, EIS)³⁷ and thus an optical nonlinearity that is detected at the exciton resonance. To check the effect of such many-body interactions on the 2DES lineshapes of our CsPbBr₃ crystals, we have investigated the pump-fluence dependence of the 2DES maps (Fig. S4). The dispersive exciton diagonal peak and free-carrier-induced vertically elongated cross-peak slightly broaden along the E_D with increasing pump-fluence, consistent with EID, whereas no significant peak distortion, i.e., a transition in lineshape from dispersive to absorptive, is observed. Such a peak distortion could have reflected strong EIS³⁸. Instead, the lineshapes remain dispersive over the investigated fluence range up to 20 $\mu\text{J}/\text{cm}^2$ (Fig. S4a–e). At this high fluence, however, the signal amplitude A_{2D} starts to saturate (Fig. S4f), a signature that the photoexcited carrier density approaches the Mott transition³³. For the low fluence of 4 $\mu\text{J}/\text{cm}^2$, at which we conduct the experiments reported in the present manuscript, the exciton peak lineshape is dominated by bleaching and thus the dispersive shape of the peak primarily results from measuring the crystals in reflection³³. Many-body interactions, specifically EID, contribute to the nonlinear spectrum as revealed by the presence of the vertically elongated cross-peak, but they are not the dominant nonlinearity for the exciton lineshape under our experimental conditions.

From the increase in cross-peak linewidth with excitation fluence (Fig. S4 and ref. ³³), we deduce that EID dominates the cross-peak whereas EIS is weak under our experimental conditions. Similar EID-induced vertically elongated cross-peaks have been previously observed also in GaAs quantum wells³⁹.

We now focus on the 1s exciton peak. Around its center, we detect a weak subpeak structure with cross-peaks spaced by ~38 meV (Fig. 1c–e, labeled 2–6). These cross-peaks are clearly pronounced on the higher energy side of the exciton diagonal peak, yet less well resolved on the lower energy side (Fig. 1c, d, insets). This asymmetry is evidenced in the cross-sections of the 2DES map along E_X (Fig. 1c) and E_D (Fig. 1d) taken at the exciton position. The absorption coefficient of similar CsPbBr₃ single crystals was recently estimated using the optical constants obtained by spectroscopic ellipsometry⁴⁰. At room temperature, this spectrum shows the excitonic 1s peak at ~2.41 eV, in agreement with our previous 2DES study³³. In the room

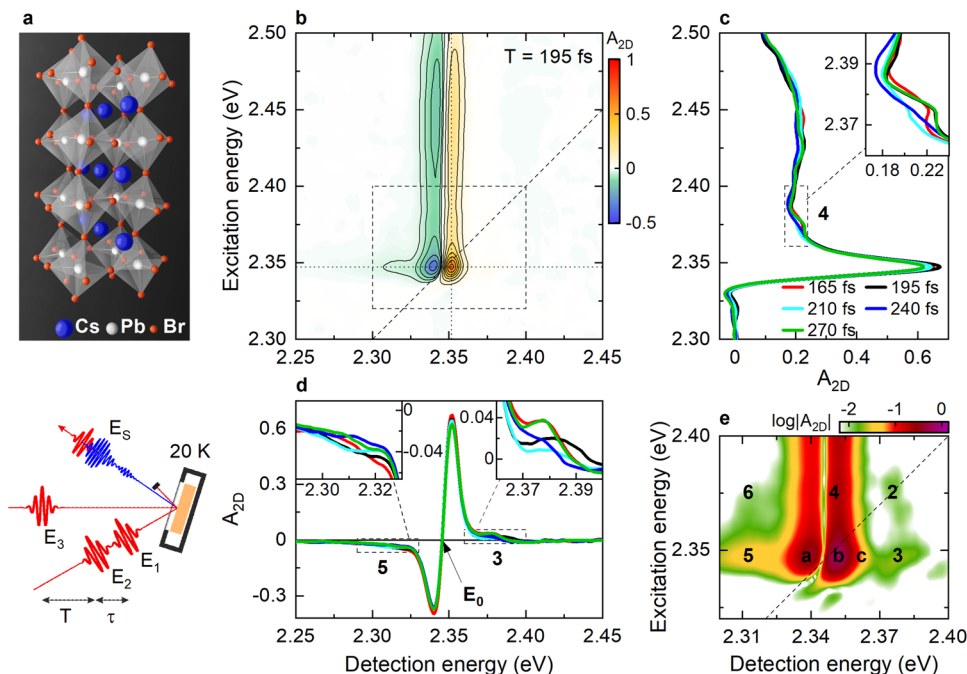


Fig. 1 | Reflection two-dimensional electronic spectroscopy (2DES) of CsPbBr₃ single crystals at 20 K. **a** CsPbBr₃ single crystals (ball-and-stick representation, upper panel) are resonantly excited and probed by a sequence of three ultrashort optical pulses (E_1 , E_2 , E_3), time-delayed by the coherence time τ and the waiting time T (lower panel). **b** 2DES map at $T = 195$ fs showing a dispersive exciton diagonal peak at $E_0 = 2.345$ eV and a vertically elongated free-carrier-induced cross-peak.

c, d Cross-sections at a fixed (c) detection and (d) fixed excitation energy, indicated by the dotted lines in b, and for selected waiting times, reveal weak vibronic cross-peaks (3, 5) with a spacing of -38 meV (310 cm⁻¹) and amplitude oscillations mainly on the high-energy peaks (3, 4 in the insets in d, c, respectively). **e** A logarithmic scale plot of the exciton region highlights the subpeak structure (2–5).

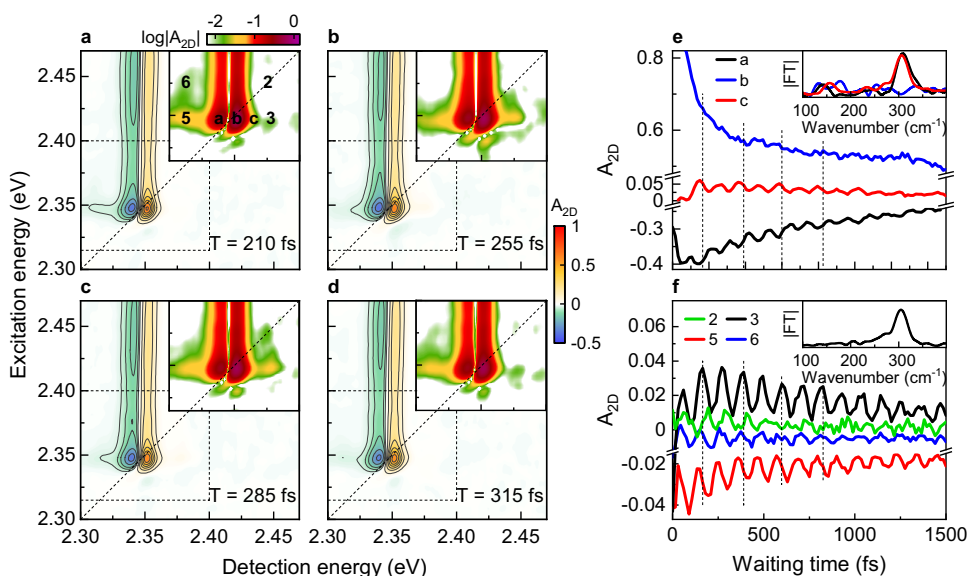


Fig. 2 | Waiting time dynamics of selected peaks in the 2DES maps reveal 310 cm⁻¹ peak amplitude oscillations that are assigned to intra-exciton Rabi oscillations. **a–d** 2DES maps at selected waiting times T between 210 fs and 315 fs. A zoom into the exciton region on a logarithmic scale (insets) shows the oscillation of the subpeak structure. **e, f** Waiting time dynamics of selected peaks near the

exciton resonance display amplitude oscillations of the A_{2D} signal with a period of 107 fs (310 cm⁻¹), matching the spectral peak spacings (see also Fig. 1), but none of the phonon modes of these crystals. The insets show the Fourier transforms of selected dynamics.

temperature data, however, no substructure can be seen due to the broad lineshapes.

2DES maps at selected waiting times are shown in Fig. 2a–d with logarithmic scale insets around the exciton region highlighting the subpeak structure. The waiting time dynamics of the A_{2D} signal at

positions a and c, i.e., at the minimum (a) and on the high-energy side (c) of the dispersive 1s exciton peak, respectively, display amplitude oscillations with 107 fs period (310 cm⁻¹ \approx 38 meV) for $T < 2$ ps (Fig. 2e, black and red). The amplitude of these oscillations nearly vanishes at the maximum of the dispersive exciton resonance, $E_0 + \delta$

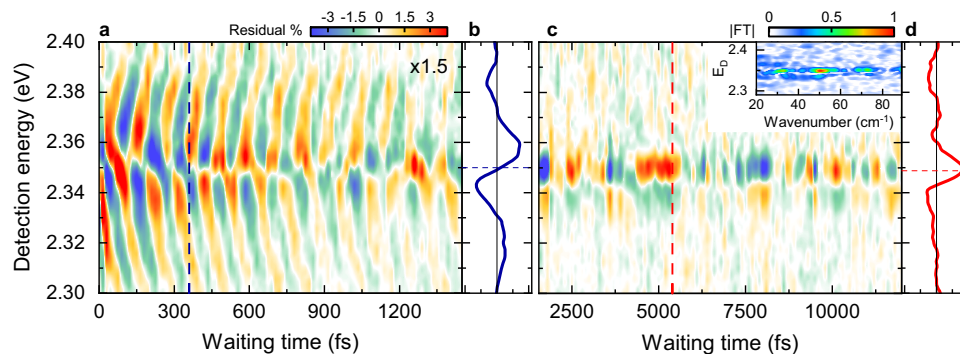


Fig. 3 | Residual map showing the oscillatory modulation of the A_{2D} signal averaged along the exciton region. **a, b** For $T < 2$ ps (**a**), the residuals show fast, 107 fs (310 cm^{-1}) oscillations and (**b**) a dispersive lineshape centered around the maximum of the 2DES cross-section (cf. Figure 1d) at $E_0 + \delta$ (dashed line in **b**). **c, d** For $T > 2$ ps (**c**), oscillations at -30 cm^{-1} and 50 cm^{-1} (FT map in the inset. See also

Figs. S5, 6) with (**d**) an absorptive lineshape centered around E_0 (dashed line in **d**) are observed. This lineshape matches the predictions of a displaced harmonic oscillator model, showing that the oscillations reflect low-frequency coherent phonon wavepacket motion. The fast oscillations in (**a**) go beyond the displaced harmonic oscillator model and are assigned to intra-exciton Rabi oscillations.

(b, Fig. 2e blue), with $\delta = 4\text{ meV}$. Pronounced amplitude oscillations at 310 cm^{-1} with an amplitude larger than 2% of the maximum A_{2D} signal are also observed at the subpeaks (Fig. 2f).

Oscillatory dynamics of the excitonic peaks amplitude

To analyze the modulation of the exciton dynamics, we isolate the oscillatory part of the A_{2D} signal by averaging along E_x around the exciton spectral region (Fig. 1b, dashed square) and subtracting a slowly decaying bi-exponential background. The obtained residual map (Fig. 3) is dominated by the 310 cm^{-1} oscillations for $T < 2$ ps (Fig. 3a). At later times, two different, lower frequency components at $\sim 30\text{ cm}^{-1}$ and 50 cm^{-1} are observed (Fig. 3c and Figs. S5, 6), corresponding to the Pb-Br-Pb bending and stretching modes of the HaP octahedra^{14,17}. The spectral shape of the residual map along E_D is clearly different at early and later times. For $T < 2$ ps, we observe a dispersive-like shape of the residual map (Fig. 3b) centered around the maximum of the exciton signal at $E_0 + \delta$ (dashed line). Its lineshape is very similar to the A_{2D} cross-section (Fig. 1d). At later times instead, the spectral dependence of the residual map for the low-frequency modes displays a symmetric, absorptive-like profile (Fig. 3d). This lineshape is consistent with that of conventional displaced harmonic oscillator (DHO) models⁴¹ for the coupling between the 1s exciton and the low-frequency phonon modes in the crystal (Fig. S8c).

Our 2DES data show distinct signatures of the coupling of excitons to persistent coherent phonons of the Pb-Br sublattice in CsPbBr₃. In the Fröhlich model, the difference between the spatial charge density distribution of electron and hole forming the exciton⁴² determines the exciton-phonon coupling strength. This results in a finite dimensionless displacement Δ of the 1s exciton potential energy surface along the phonon coordinate with respect to the ground-state equilibrium configuration (Fig. S7a). Concurrently, it leads to a reduction of the 1s exciton energy by $\Delta^2 E_V = S E_V$, with E_V being the phonon energy and S the Huang-Rhys factor⁴². In general, the exciton-phonon coupling manifests itself in characteristic phonon side-peaks around the exciton resonance in the optical spectra, provided that the phonon mode energy E_V is large enough compared to the homogeneous linewidth defined by the exciton dephasing time T_2 . Impulsive resonant optical excitation with optical pulses that are shorter in duration than the phonon period launches a coherent wavepacket onto the 1s exciton potential which oscillates in time with phonon frequency E_V/\hbar (Fig. S7c). For the 30 and 50 cm^{-1} oscillations, E_V is smaller than the homogeneous linewidth of the exciton resonance $2\hbar/T_2$. In this limit, the side-peaks are not resolved and the wavepacket motion results in a periodic modulation of the exciton resonance $E_0(T) = E_0 - \Delta^2 E_V [1 - \cos(E_V T/\hbar)]$. In the 2DES maps, this leads to a

small, periodic shift of the dispersive exciton lineshape along E_D , with an energy shift that is much smaller than the resonance linewidth. In the residual maps, we plot the difference between the 2DES map at a given T and that averaged over one oscillation period. Therefore, the lineshape of the residuals is given by the derivative of the $A_{2D}(T)$ signal with respect to E_D . This results in absorptive lineshapes of the residuals along E_D (Fig. S8c) matching those in Fig. 3c. The amplitude of the residuals oscillates with the phonon frequency, changing sign at every half period. This amplitude provides a good estimate of Δ and we deduce values between 0.1 and 0.2, thus small $S \leq 0.04$, for the two phonon modes. Altogether, this confirms that the low-frequency oscillations in Fig. 3c reflect impulsive excitation of coherent phonon wavepackets induced by exciton-phonon coupling in our CsPbBr₃ crystals.

For $T < 2$ ps instead, the dispersive shape of the residual map for the 310 cm^{-1} oscillations clearly does not fit to this model. If the 310 cm^{-1} oscillation was an optical phonon mode of the crystal, which we checked it is not, then $E_V > 2\hbar/T_2$ and the coherent wavepacket motion should give rise to distinct side-peaks in the nonlinear optical spectra (Fig. S8b) with amplitudes oscillating periodically in time. Such side-peak oscillations, however, could not explain the dispersive lineshape of the residuals observed in Fig. 3a (cf. Fig. S8d). Moreover, we note that the point labeled 5 in Fig. 1d, e is on the tail of the dispersive main exciton peak lineshape and is not a cross-peak. It oscillates nearly in phase with the oscillating main exciton peak, in contrast to expectations of a DHO model.

Dark excitons, arising from exciton fine structure splittings, have been reported slightly below the bright 1s exciton in HaPs⁴³. The energy splittings between the bright and low-lying dark excitons in bulk HaPs are however of the order of only $\sim 2\text{ meV}$ ^{43,44}, thus much smaller than the observed $\sim 38\text{ meV}$ (310 cm^{-1}) splittings between the main exciton and side-peaks in our 2DES maps. Moreover, the side-peaks in our 2DES maps are clearly on the high-energy side of the 1s exciton resonance. Therefore, we can rule out that lower-lying dark states from exciton fine structure splittings give rise to the observed spectral substructure.

Based on this analysis, the DHO model is unable to explain our observations (Fig. 3a). Weak resonances $\sim 300\text{--}320\text{ cm}^{-1}$ observed in Raman studies^{45–47} have been tentatively assigned to an overtone of the 150 cm^{-1} mode, the highest frequency optical phonon in CsPbBr₃¹⁷. In our 2DES data we do not detect any significant amplitude oscillation at 150 cm^{-1} nor any phonon side-peaks associated with this frequency. Moreover, control measurements of layered 2D-HaPs, namely $(\text{BA})_2(\text{MA})_{n-1}\text{Pb}_n\text{I}_{3n+1}$ with $n = 3$ and $\text{BA} = \text{CH}_3(\text{CH}_2)_3\text{NH}_3$ as the organic spacer, having similar low-frequency phonon modes as CsPbBr₃, but

substantially larger exciton binding energy⁴⁸, show neither 310 cm⁻¹ oscillations nor dispersive shape of the residual map, but only low-frequency lead-halide phonon oscillations with residuals matching the DHO (Fig. S9b). As such, we exclude that the observed 310 cm⁻¹ oscillation in our CsPbBr₃ data arises from a phonon overtone.

Temporal oscillations with frequencies higher than coherent phonons have been recently observed in CsPbBr₃ for excitation energies below the optical bandgap in 2D-optical Kerr effect experiments in transmission⁴⁹. Those oscillations were attributed to birefringence arising from an instantaneous, off-resonant nonlinear optical response induced by the pump pulses^{49,50}. In contrast, in our 2DES experiments, the high-frequency 310 cm⁻¹ oscillations arise from a resonant non-linearity of the crystals and appear only for excitation and detection energies around the exciton resonance. Potential contributions of birefringence-induced below-bandgap oscillations as discussed in ref. 49 are not relevant under our experimental conditions.

THz-pump-VIS-probe studies of MAPbI₃ thin films observed a transient shift of the optical bandgap and temporal oscillations in the differential transmission amplitude resulting from the coupling of the Pb-I bending mode at 1 THz to the crystal bandgap¹⁵. In contrast to our 2DES experiment, the THz pump resonantly and selectively excites low-frequency phonon modes, but it does not excite electronic populations, i.e., excitons or free carriers. It instead induces phonon coherences in the crystal ground state. This results in an oscillatory, strain-induced change in the bandgap of the material that is probed by the time-delayed visible probe pulse. In contrast, here we do not selectively excite specific phonon modes of our CsPbBr₃ crystals and hence the observed low-frequency phonon wavepacket motion (Fig. 3c and S5d) reveals the Pb-Br modes that most strongly couple to the exciton. Most importantly, within the first -2 ps, we observe oscillations with much higher frequencies (Figs. 2e, f and 3a) than those reported in ref. 15.

All this raises questions about the origin of the observed 310 cm⁻¹ amplitude oscillations. Exciton resonance energy oscillations with 310 cm⁻¹ frequency would still result in absorptive-like spectral shape of the residuals and thus cannot account for the observed dispersive shape in Fig. 3a. The latter may be caused by a change either in the exciton population or in the exciton transition dipole moment⁵¹. Changes in the exciton transition dipole moment, however, will not give rise to side-peaks in the optical spectra. Here, we propose that the low-frequency phonon modes in the CsPbBr₃ not only couple to the 1s exciton, but also drive dipole-allowed transitions to higher-lying exciton states resulting in coherent oscillations of the exciton population. These oscillations modulate the exciton peak amplitude in 2DES leading to the dispersive shape of the residuals.

Discussion

Within the three-dimensional exciton hydrogen-like progression commonly assumed for bulk HaPs⁴³, the lowest-lying resonance is a 1s exciton carrying the largest oscillator strength, whereas higher-lying s-states are much weaker. Excited-state transitions between s-states are dipole forbidden and thus signatures of higher-lying s-states could only appear in weak diagonal peaks, but cannot explain the cross-peaks nor their oscillations in our 2DES data. Within such a hydrogen-like model, transitions between the 1s exciton and the higher-lying optically dark 2p exciton are dipole allowed. They may be driven by external THz fields^{52,53} or, as we argue here, by the internal electric field associated with the low-frequency phonons inside the crystals. In CsPbBr₃, where the exciton binding energy for the lowest energy exciton (1s) is 40 meV³⁶, the energy splitting between 1s and 2p is $\Delta E_{1s,2p} \approx 30$ meV. Thus, in principle, the low-frequency phonon fields can off-resonantly drive transitions between them. This implies that they can induce a periodic transfer of a small fraction of the 1s exciton population to the 2p exciton state and back. Consequently, population oscillations between the exciton states transiently modulate the

excitonic optical absorption of the crystal at a frequency governed by the splitting between the coupled states. In the nonlinear optical spectra, this will result in side-peaks of the 1s exciton and peak amplitude oscillations with frequencies determined by the population oscillations. The coupling strength inducing such splitting is governed by the dipole coupling $\hbar\Omega \approx \mu_{1s,2p} E_{ph}$, with $\mu_{1s,2p}$ being the amplitude of the 1s-2p-transition dipole moment and E_{ph} the phonon field amplitude. An estimation of $\mu_{1s,2p}$ based on the overlap integral of hydrogenic 1s and 2p wavefunctions, and of E_{ph} results in a coupling strength of $\hbar\Omega \approx 8$ meV, a factor of two larger than the value deduced from our experiments (Supplementary Note 2, 2.2.1). This is -27% of the bare 1s-2p energy splitting $\Delta E_{1s,2p}$, suggesting that this exciton-phonon field dipole coupling in CsPbBr₃ crystals can reach the ultrastrong coupling limit, in analogy to light-matter couplings⁵⁴.

Since $\Delta E_{1s,2p} \approx 5E_V$, the phonon field drives the 1s-2p transition off-resonantly. As such, the rotating wave approximation (RWA), usually adopted in the Jaynes-Cummings model, is not justified, and the full exciton-phonon field interaction has to be considered. This includes both RWA terms and counter-rotating (CR) terms of the interaction (Supplementary Note 2, 2.2.2). The RWA terms promote energy-conserving transitions between $|1s, \nu + 1\rangle$ and $|2p, \nu\rangle$, where $|n, \nu\rangle$ are vibronic states in a non-displaced basis with $n = 1s, 2p$ and $\nu = 0, 1, 2, \dots$ being the vibrational quantum number. The CR terms induce transitions between $|1s, \nu\rangle$ and $|2p, \nu + 1\rangle$ vibronic states and thus promote the excitonic transitions from the 1s to 2p manifold (or 2p to 1s) while concurrently creating (or destroying) a phonon quantum. We argue that here those CR terms even dominate the coupling and result in the observed 310 cm⁻¹ oscillations.

To support this argument, we simulate the exciton optical response of the CsPbBr₃ crystals using a three-state DHO model (Fig. 4a) including the crystal ground-state, the 1s and 2p excitons, and the dipole coupling between them via a quantized 50 cm⁻¹ ($E_V = 6.3$ meV) phonon field based on the full exciton-phonon field interaction. In this simplified picture (Fig. 4a), we restrict our model to excitons at $k = 0$ in momentum space and neglect higher k-states. This approximation is reasonably well justified since our experimental data show essentially no disorder-induced inhomogeneous broadening. Thus, the optical pulses can only couple to excitons with wavevector $k \approx 0$, whereas transitions to optically dark higher k-states excitons are negligible to a first approximation. In this model, the impulsive optical excitation launches coherent phonon wavepackets oscillating with 50 cm⁻¹ frequency on the optically bright 1s exciton potential energy surface. The phonon field drives the dipole-allowed transition between 1s and 2p with $V_{ep} = \hbar\Omega\sqrt{\nu+1}$ (Supplementary Note 2, 2.2.2). We find good agreement between simulation and experiment for $\hbar\Omega = 3.7$ meV. The coupling induces hybridization of $|1s, \nu\rangle$ and $|2p, \nu\rangle$ vibronic states which, upon optical excitation of the 1s exciton, leads to Rabi oscillations between the populations, n_{1s} and n_{2p} , of 1s and 2p excitons (Fig. 4b). Since the displacement of the 1s exciton potential energy surface is small, the optical excitation mainly populates $|1s, 0\rangle$, and weakly $|1s, 1\rangle$, whereas the population of higher-lying $|1s, \nu > 1\rangle$ states is negligible (Fig. S7b). RWA interaction terms cannot induce couplings between $|1s, 0\rangle$ and the 2p manifold (Figs. S10 and S11c) and thus they cannot give rise to the oscillations of n_{1s} and n_{2p} in Fig. 4b. The dominant frequency (307 cm⁻¹, Fig. 4b inset) of these oscillations arises from the energy splitting between hybridized 1s and 2p vibronic states involving $|1s, 0\rangle$. In the range of $\hbar\Omega$ considered here, the lowest-lying 1s-2p-phonon eigenstate can be approximated as arising from the hybridization of mainly $|1s, 0\rangle$ and $|2p, 1\rangle$ with the contributions of other higher-lying 1s and 2p vibronic states being negligible. Therefore, the dominant contribution to the splitting, and hence to the population oscillations, arises from the CR-induced coupling between $|1s, 0\rangle$ and $|2p, 1\rangle$ (Fig. S12). Thus CR terms of the interaction are necessary to explain our data.

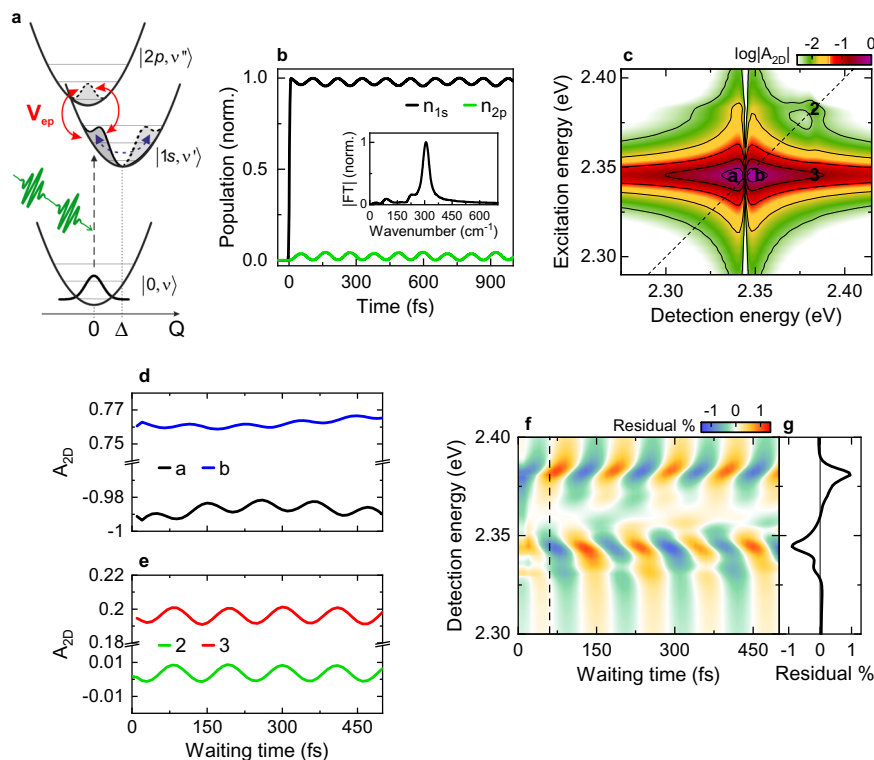


Fig. 4 | Model simulations of phonon-driven intra-exciton Rabi oscillations in CsPbBr₃ crystals. **a** Displaced harmonic oscillator model including the bright $|1s, \nu'\rangle$ and dark $|2p, \nu''\rangle$ exciton states, with $\nu', \nu'' = 0, 1, 2, \dots$, the vibrational quantum number associated with the 50 cm^{-1} phonon mode. We include the dipole coupling between 1s and 2p via a quantized phonon field driving Rabi oscillations between them. The coupling V_{ep} is governed by the 1s–2p transition dipole moment and by the phonon field. **b** Simulated dynamics of the electronic 1s (black) and 2p (green) populations n_{1s} and n_{2p} . The dynamics of those populations show Rabi oscillations with a dominant period of $\sim 109 \text{ fs}$ (307 cm^{-1}), as seen by taking the Fourier

transform of n_{1s} (inset). **c** An exemplary simulated 2DES map at $T = 80 \text{ fs}$ (logarithmic scale plot) reveals high-energy side-peaks (2, 3) with spacings of $\sim 38 \text{ meV}$ (307 cm^{-1}) arising from the mixing of 1s and 2p vibronic states induced by the phonon mode. **d, e** In the waiting time dynamics, this coupling leads to peak amplitude oscillations with a period of $\sim 109 \text{ fs}$ and with similar distribution as the amplitude modulation in the experiment. **f, g** The residual map shows a dispersive-like spectral profile along the detection energy axis, in good agreement with that observed in the experiments.

In the 2DES maps, this coupling results in diagonal peaks at the energies of the bright eigenstates and their cross-peaks. The strongest diagonal peak marks the lowest-lying bright eigenstate which mainly arises from the mixing of $|1s, 0\rangle$ and $|2p, 1\rangle$ and it is approximately at the energy of the ground-state-to- $|1s, 0\rangle$ transition. This is the main diagonal exciton peak at 2.345 eV (Fig. 4c and Fig. 1e). The other, weaker diagonal peak arises from the brightening of the ground-state-to- $|2p, 1\rangle$ transition upon coupling and gives rise to the weak diagonal peak at position 2 in the 2DES maps (Figs. 4c and 1e). As such, in the 2DES maps we observe a main diagonal peak at approximately the energy of the 1s exciton transition, a second much weaker diagonal peak approximately around the $|2p, 1\rangle$ transition, and their cross peaks, in agreement with our experimental observations.

Population oscillations result in a periodic modulation of the nonlinear optical polarization, which leads to weak vibronic side-peaks on the high-energy side of the exciton resonance in the 2DES maps (Fig. 4c and Fig. S13b). The spacing between the side-peak and the main peak reflect the energy splittings discussed above. In the dynamics, $\sim 109\text{-fs}$ peak amplitude oscillations (Fig. 4d, e) appear, matching the peak spacings. The resulting residual map (Fig. 4f) shows a dispersive-like spectral profile with a sign change around the maximum of the exciton lineshape (Fig. 4g and Fig. S13), in agreement with the experiments. We note that the position at which the oscillations are most strongly reduced is not at the zero-crossing of the dispersive exciton resonance, but around its maximum in both simulation and experiment (indicated as peak b in Figs. 4c and 1d, e). This is because the Rabi oscillations do not occur between two purely electronic states but

involve higher-lying vibronic 1s and 2p manifolds. Importantly, the frequency of these phonon-induced intra-exciton Rabi oscillations (Fig. 4b) is not simply a multiple of the phonon frequency, but reflects the energy splitting between the coupled $|1s, 0\rangle$ and $|2p, 1\rangle$ states, i.e., hybridized 1s–2p-phonon modes induced by CR terms. This is fundamentally different from the Fröhlich coupling. For a coupling strength $\hbar\Omega = 3.7 \text{ meV}$, $\hbar\Omega/\Delta E_{1s,2p} = 0.12$ which is on the onset of the ultrastrong coupling regime⁵⁴. Our results thus imply that the quantum nature of the phonon fields in HaPs may play an important role for this exciton-phonon coupling in analogy to light-matter couplings^{1,54,55}.

In our model we assume that only the 50 cm^{-1} mode is responsible for the coupling. This is a reasonable approximation since the detuning between the mode energy E_V and $\Delta E_{1s,2p}$ is smaller than for the 30 cm^{-1} mode. From our 2DES data we estimate similar Huang-Rhys factors for both phonon modes. Thus, a larger coupling strength for the 30 cm^{-1} mode is needed to compete with Rabi oscillations induced by the 50 cm^{-1} mode. As such, while we cannot strictly rule out that also the 30 cm^{-1} phonon mode is involved in the coupling, we expect that the 50 cm^{-1} mode dominates.

The phonon-induced electric fields in the crystals can promote off-resonant Rabi oscillations between $|1s, \nu'\rangle$ and $|2p, \nu''\rangle$ vibronic states only as long as the coherence between them is maintained. Thus, the dephasing between those vibronic states determines the dephasing of the Rabi oscillations. Since the phonon dephasing ($\sim 7\text{--}8 \text{ ps}$ at 20 K) is much longer than the timescale over which we observe Rabi oscillations ($\sim 2 \text{ ps}$), our results suggest that the decay of the Rabi oscillations can be taken as a measure of the dephasing time between 1s and 2p

excitonic manifolds. As such, the revealed Rabi oscillations may offer a way to study the dephasing mechanisms within the excited exciton manifold which is important, e.g., for applications in light-emission.

Our results also suggest that for materials with similar low-frequency phonon spectra as CsPbBr₃, the exciton binding energy can be used to control the Rabi oscillations dynamics and thus the transient excitonic response. Specifically, larger exciton binding energies in the presence of a similar phonon spectrum result in larger 1s-2p splitting and thus larger detuning with the phonon mode energy. Based on our model, we thus expect no significant Rabi oscillations in this scenario. This is confirmed by the results of control measurements on layered 2D-HaPs (Fig. S9) having an exciton binding energy more than four times larger⁴⁸ compared to bulk CsPbBr₃ but a similar low-frequency phonon spectrum of the lead-halide lattice⁵⁶.

In conclusion, we have shown that in CsPbBr₃ single crystals, internal electric fields generated by low-frequency phonon modes induce mixing of 1s and 2p excitons leading to Rabi oscillations for up to ~2 ps at 20 K. These intra-exciton Rabi oscillations cannot be explained by conventional models for electron-phonon couplings in the adiabatic regime. The disclosed mechanism can crucially contribute to explain the strongly anharmonic response of HaPs and, in relation to that, the plethora of peculiar behaviors exhibited by these materials^{57,58}. Importantly, the reported observations call for the development of new theoretical approaches beyond the status quo models originally developed for conventional semiconductors, which in spite of their applicability to HaPs as demonstrated also in this work, still fundamentally rely on the Born-Oppenheimer approximation. Only in this way, it will be possible to fully unfold the behavior of this emerging class of materials not only as candidates for next-generation optoelectronic devices, but also as platforms to study light-matter phenomena in the strong and ultrastrong coupling regime.

Methods

CsPbBr₃ crystal synthesis and characterization

Powders of cesium bromide (CsBr) (Aldrich, 99.999%) without further purification and lead-bromide (PbBr₂) (Aldrich, ≥98%) that was dried in a vacuum oven overnight, were dissolved in dimethylsulfoxide (DMSO) (Aldrich, ≥99.9%). Acetonitrile (MeCN) (BioLab LTD, HPLC grade, 99.97%) and methanol (MeOH) (BioLab LTD, HPLC grade, 99.95%) were used as received. A 0.45 M solution (slightly below the ~0.5 M solubility limit) of the perovskite precursors (equimolar amounts of CsBr and PbBr₂) in the same solution of DMSO was prepared in ambient air (ca. 45% RH) under continuous stirring at -50 °C, until no powder is observed. It is important to mix the precursors in the same volume, because the room temperature solubility limit of CsBr in DMSO is ca. 0.25 M when it is dissolved separately. After cooling to room temperature, the DMSO solution was titrated (drop-wise under continuous stirring) with MeCN. During the titration, a yellow-orange precipitant appeared with addition of each drop and quickly re-dissolved. As the system gets closer to the saturation point (more pronounced when MeCN is added), a permanent white solid precipitates. At MeCN: DMSO ratios of 1.1:1 the yellow-orange precipitate no longer re-dissolved. These saturated solutions were thoroughly sealed (to prevent loss of the volatile MeCN) and stirred for 24 hours at 50 °C. After heating for 24 h, a pale green-yellow strongly-fluorescent precipitant was clearly observed along-side the other precipitated species. The saturated solutions can be further stored (best in the dark) for at least several months, until their use for crystal growth. Before crystal growth, the saturated precursor solutions are filtered with PTFE 0.2 μm pore-size syringe filters. No noticeable differences in crystal growth or kinetics were observed between properly stored or freshly prepared solutions.

The filtered precursor solutions were placed in a clean crystallization flask and covered with a filter paper and a glass petri-dish on top to limit anti-solvent vapor diffusion. The covered crystallization

flask was then placed inside a deeper, flat-bottomed, glass dish, which contained MeCN (anti-solvent). The setup was left at ambient conditions in a quiet location for further growth. After ~2–3 days the crystals were taken out. Typical single crystals were collected from the crystallization solution. The crystallographic orientations are verified via XRD analysis in a specular reflection mode, where the (101) plane is set as the reflection plane. For further details see ref.⁵⁹.

Two-dimensional electronic spectroscopy

We perform low-temperature two-dimensional electronic spectroscopy (2DES) in reflection using a home-built setup in the partially collinear geometry as detailed in ref.³³. Briefly, the broadband optical pulses, with a spectrum ranging from -2.00 eV to -2.55 eV (Fig. S1), are generated by a home-built non-collinear optical parametric amplifier (NOPA), pumped by the second-harmonic of a regeneratively amplified Ti:Sapphire laser (Spectra Physics Spitfire Pro, 5 kHz repetition rate). Chirped mirrors (Laser Quantum DCM9) are used to pre-compress the pulses. The phase-locked pump pulse pair used for the excitation is generated by a TWINS^{60,61} interferometer consisting of α-BBO wedges. The dispersion introduced by the wedges is compensated by an additional pair of chirped mirrors (Laser Quantum DCM9) introduced in the pump arm of the setup. To scan the coherence time τ (i.e., the time delay between the two pump pulses) and the waiting time T (time delay between the second pump and probe pulse), we use motorized delay stages (Physik Instrumente MI12.1DG, M413.2DG). During each measurement, we monitor τ by recording the auto-correlation of the two pump pulses with a photodiode before the sample. Pump and probe beams are focused onto the sample through the quartz window of a cryostat (KONTI Micro, CryoVac), each to a round spotsize of ~120 μm in diameter, using spherical mirrors before the cryostat. The beam area is carefully characterized with a beam camera (Thorlabs DCC1545M-GL). During the measurements, the sample is kept at 20 K in the cryostat. The probe beam reflected from the sample is dispersed into a monochromator and collected with a high-speed CCD line camera (e2v AviiVa EM4).

The measured differential reflection from the sample as a function of τ and T and of the detection energy E_D is given by $\frac{\Delta R}{R}(\tau, T, E_D) = \frac{R_{on}(\tau, T, E_D) - R_{off}(E_D)}{R_{off}(E_D)}$, with R_{on} and R_{off} the reflected probe spectra with the pump on and off, respectively. By taking the real part of the Fourier transform of the measured $\Delta R/R$ signal along τ , we obtain the 2DES energy-energy maps $A_{2D}(E_X, T, E_D)$ at each T as a function of E_D and of the excitation energy E_X . To characterize the time resolution of the setup, we record second-harmonic generation frequency-resolved optical gating (SHG-FROG) maps of the cross-correlation between pump and probe arms outside the cryostat introducing an additional quartz window into the beam path to account for the window of the cryostat. This allows us to compensate the chirp introduced by the window of the cryostat with chirp mirrors before the setup. The recorded SHG-FROG map after chirp compensation indicates a time resolution of ~13 fs (Fig. S1). For all measurements shown in the main manuscript, the excitation fluence is set to 4 μJ/cm².

Data availability

The data that support the findings of this study are available from the authors upon request.

References

1. Garcia-Vidal Francisco, J., Ciuti, C. & Ebbesen Thomas, W. Manipulating matter by strong coupling to vacuum fields. *Science* **373**, eabd0336 (2021).
2. Kowalewski, M. & Mukamel, S. Manipulating molecules with quantum light. *Proc. Natl Acad. Sci.* **114**, 3278 (2017).
3. Hutchison, J. A., Schwartz, T., Genet, C., Devaux, E. & Ebbesen, T. W. Modifying chemical landscapes by coupling to vacuum fields. *Angew. Chem. Int. Ed.* **51**, 1592–1596 (2012).

4. Orgiu, E. et al. Conductivity in organic semiconductors hybridized with the vacuum field. *Nat. Mater.* **14**, 1123–1129 (2015).
5. Feist, J. & Garcia-Vidal, F. J. Extraordinary exciton conductance induced by strong coupling. *Phys. Rev. Lett.* **114**, 196402 (2015).
6. Herrera, F. & Spano, F. C. Cavity-controlled chemistry in molecular ensembles. *Phys. Rev. Lett.* **116**, 238301 (2016).
7. Schneider, C., Glazov, M. M., Korn, T., Höfling, S. & Urbaszek, B. Two-dimensional semiconductors in the regime of strong light-matter coupling. *Nat. Commun.* **9**, 2695 (2018).
8. Schäfer, C., Ruggenthaler, M., Appel, H. & Rubio, A. Modification of excitation and charge transfer in cavity quantum-electrodynamical chemistry. *Proc. Natl Acad. Sci.* **116**, 4883 (2019).
9. Cortese, E. et al. Excitons bound by photon exchange. *Nat. Phys.* **17**, 31–35 (2021).
10. Thompson, R. J., Rempe, G. & Kimble, H. J. Observation of normal-mode splitting for an atom in an optical cavity. *Phys. Rev. Lett.* **68**, 1132–1135 (1992).
11. Vasa, P. et al. Real-time observation of ultrafast Rabi oscillations between excitons and plasmons in metal nanostructures with J-aggregates. *Nat. Photonics* **7**, 128–132 (2013).
12. Franchini, C., Reticcioli, M., Setvin, M. & Diebold, U. Polarons in materials. *Nat. Rev. Mater.* **6**, 560–586 (2021).
13. Feynman, R. P. Slow electrons in a polar crystal. *Phys. Rev.* **97**, 660–665 (1955).
14. Miyata, K. et al. Large polarons in lead halide perovskites. *Sci. Adv.* **3**, e1701217 (2017).
15. Kim, H. et al. Direct observation of mode-specific phonon-band gap coupling in methylammonium lead halide perovskites. *Nat. Commun.* **8**, 687 (2017).
16. Park, M. et al. Excited-state vibrational dynamics toward the polaron in methylammonium lead iodide perovskite. *Nat. Commun.* **9**, 2525 (2018).
17. Yaffe, O. et al. Local polar fluctuations in lead halide perovskite crystals. *Phys. Rev. Lett.* **118**, 136001 (2017).
18. Herz, L. M. How lattice dynamics moderate the electronic properties of metal-halide perovskites. *J. Phys. Chem. Lett.* **9**, 6853–6863 (2018).
19. Ghosh, D., Welch, E., Neukirch, A. J., Zakhidov, A. & Tretiak, S. Polarons in halide perovskites: a perspective. *J. Phys. Chem. Lett.* **11**, 3271–3286 (2020).
20. Fröhlich, H. Electrons in lattice fields. *Adv. Phys.* **3**, 325–361 (1954).
21. Wright, A. D. et al. Electron–phonon coupling in hybrid lead halide perovskites. *Nat. Commun.* **7**, 11755 (2016).
22. Bretschneider, S. A. et al. Quantifying polaron formation and charge carrier cooling in lead-iodide perovskites. *Adv. Mater.* **30**, 1707312 (2018).
23. Batignani, G. et al. Probing femtosecond lattice displacement upon photo-carrier generation in lead halide perovskite. *Nat. Commun.* **9**, 1971 (2018).
24. Thouin, F. et al. Phonon coherences reveal the polaronic character of excitons in two-dimensional lead halide perovskites. *Nat. Mater.* **18**, 349–356 (2019).
25. Puppini, M. et al. Evidence of large polarons in photoemission band mapping of the perovskite semiconductor CsPbBr₃. *Phys. Rev. Lett.* **124**, 206402 (2020).
26. Evans, T. J. S. et al. Competition between hot-electron cooling and large polaron screening in CsPbBr₃ perovskite single crystals. *J. Phys. Chem. C* **122**, 13724–13730 (2018).
27. Srimath Kandada, A. R. & Silva, C. Exciton polarons in two-dimensional hybrid metal-halide perovskites. *J. Phys. Chem. Lett.* **11**, 3173–3184 (2020).
28. Neukirch, A. J. et al. Geometry distortion and small polaron binding energy changes with ionic substitution in halide perovskites. *J. Phys. Chem. Lett.* **9**, 7130–7136 (2018).
29. Li, W., She, Y., Vasenko, A. S. & Prezhdo, O. V. Ab initio nonadiabatic molecular dynamics of charge carriers in metal halide perovskites. *Nanoscale* **13**, 10239–10265 (2021).
30. Schilcher, M. J. et al. The significance of polarons and dynamic disorder in halide perovskites. *ACS Energy Lett.* **6**, 2162–2173 (2021).
31. Cohen, A. V., Egger, D. A., Rappe, A. M. & Kronik, L. Breakdown of the static picture of defect energetics in halide perovskites: the case of the Br vacancy in CsPbBr₃. *J. Phys. Chem. Lett.* **10**, 4490–4498 (2019).
32. Debnath, T. et al. Coherent vibrational dynamics reveals lattice anharmonicity in organic–inorganic halide perovskite nanocrystals. *Nat. Commun.* **12**, 2629 (2021).
33. Nguyen, X. T. et al. Ultrafast charge carrier relaxation in inorganic halide perovskite single crystals probed by two-dimensional electronic spectroscopy. *J. Phys. Chem. Lett.* **10**, 5414–5421 (2019).
34. Li, H., Moody, G. & Cundiff, S. T. Reflection optical two-dimensional Fourier-transform spectroscopy. *Opt. Express* **21**, 1687–1692 (2013).
35. Ceratti, D. R. et al. The pursuit of stability in halide perovskites: the monovalent cation and the key for surface and bulk self-healing. *Mater. Horiz.* **8**, 1570–1586 (2021).
36. Protesescu, L. et al. Nanocrystals of cesium lead halide perovskites (CsPbX₃, X = Cl, Br, and I): Novel optoelectronic materials showing bright emission with wide color gamut. *Nano Lett.* **15**, 3692–3696 (2015).
37. Li, X., Zhang, T., Borca, C. N. & Cundiff, S. T. Many-body interactions in semiconductors probed by optical two-dimensional fourier transform spectroscopy. *Phys. Rev. Lett.* **96**, 057406 (2006).
38. Webber, D. et al. Signatures of four-particle correlations associated with exciton-carrier interactions in coherent spectroscopy on bulk GaAs. *Phys. Rev. B* **94**, 155450 (2016).
39. Borca, C. N., Zhang, T., Li, X. & Cundiff, S. T. Optical two-dimensional Fourier transform spectroscopy of semiconductors. *Chem. Phys. Lett.* **416**, 311–315 (2005).
40. Mannino, G. et al. Temperature-dependent optical band gap in CsPbBr₃, MAPbBr₃, and FAPbBr₃ single crystals. *J. Phys. Chem. Lett.* **11**, 2490–2496 (2020).
41. Kumar, A. T. N., Rosca, F., Widom, A. & Champion, P. M. Investigations of ultrafast nuclear response induced by resonant and non-resonant laser pulses. *J. Chem. Phys.* **114**, 6795–6815 (2001).
42. Zhang, X. B., Taliencio, T., Kolliakos, S. & Lefebvre, P. Influence of electron-phonon interaction on the optical properties of III nitride semiconductors. *J. Phys. Condens. Matter* **13**, 7053–7074 (2001).
43. Baranowski, M. & Plochocka, P. Excitons in metal-halide perovskites. *Adv. Energy Mater.* **10**, 1903659 (2020).
44. Baranowski, M. et al. Giant fine structure splitting of the bright exciton in a bulk MAPbBr₃ single crystal. *Nano Lett.* **19**, 7054–7061 (2019).
45. Cha, J.-H. et al. Photoresponse of CsPbBr₃ and Cs₄PbBr₆ perovskite single crystals. *J. Phys. Chem. Lett.* **8**, 565–570 (2017).
46. Ibaceta-Jaña, J. et al. Vibrational dynamics in lead halide hybrid perovskites investigated by Raman spectroscopy. *Phys. Chem. Chem. Phys.* **22**, 5604–5614 (2020).
47. Guo, Y. et al. Interplay between organic cations and inorganic framework and incommensurability in hybrid lead-halide perovskite CH₃NH₃PbBr₃. *Phys. Rev. Mater.* **1**, 042401 (2017).
48. Blancon, J. C. et al. Scaling law for excitons in 2D perovskite quantum wells. *Nat. Commun.* **9**, 2254 (2018).
49. Maehrlein, S. F. et al. Decoding ultrafast polarization responses in lead halide perovskites by the two-dimensional optical Kerr effect. *Proc. Natl Acad. Sci.* **118**, e2022268118 (2021).
50. Huber, L., Maehrlein, S. F., Wang, F., Liu, Y. & Zhu, X. Y. The ultrafast Kerr effect in anisotropic and dispersive media. *J. Chem. Phys.* **154**, 094202 (2021).

51. Baldini, E. et al. Phonon-driven selective modulation of exciton oscillator strengths in anatase TiO₂ nanoparticles. *Nano Lett.* **18**, 5007–5014 (2018).
52. Kaindl, R. A., Hägele, D., Carnahan, M. A. & Chemla, D. S. Transient terahertz spectroscopy of excitons and unbound carriers in quasi-two-dimensional electron-hole gases. *Phys. Rev. B* **79**, 045320 (2009).
53. Ulbricht, R., Hendry, E., Shan, J., Heinz, T. F. & Bonn, M. Carrier dynamics in semiconductors studied with time-resolved terahertz spectroscopy. *Rev. Mod. Phys.* **83**, 543–586 (2011).
54. Frisk Kockum, A., Miranowicz, A., De Liberato, S., Savasta, S. & Nori, F. Ultrastrong coupling between light and matter. *Nat. Rev. Phys.* **1**, 19–40 (2019).
55. Forn-Díaz, P., Lamata, L., Rico, E., Kono, J. & Solano, E. Ultrastrong coupling regimes of light-matter interaction. *Rev. Mod. Phys.* **91**, 025005 (2019).
56. Menahem, M. et al. Strongly anharmonic octahedral tilting in two-dimensional hybrid halide perovskites. *ACS Nano* **15**, 10153–10162 (2021).
57. Ceratti, D. R. et al. Self-healing inside APbBr₃ halide perovskite crystals. *Adv. Mater.* **30**, 1706273 (2018).
58. Cahen, D., Kronik, L. & Hodes, G. Are defects in lead-halide perovskites healed, tolerated, or both? *ACS Energy Lett.* **6**, 4108–4114 (2021).
59. Rakita, Y. et al. Low-temperature solution-grown CsPbBr₃ single crystals and their characterization. *Cryst. Growth Des.* **16**, 5717–5725 (2016).
60. Brida, D., Manzoni, C. & Cerullo, G. Phase-locked pulses for two-dimensional spectroscopy by a birefringent delay line. *Opt. Lett.* **37**, 3027–3029 (2012).
61. Réhault, J., Maiuri, M., Oriana, A. & Cerullo, G. Two-dimensional electronic spectroscopy with birefringent wedges. *Rev. Sci. Instrum.* **85**, 123107 (2014).

Acknowledgements

Financial support by the Ministry of Science and Culture (MWK) of the State of Lower Saxony and the Volkswagen Foundation (“Niedersächsisches Vorab—Research Cooperation Lower Saxony-Israel”, “Niedersächsisches Vorab—SMART”, “Professorinnen für Niedersachsen”, “DyNano”), and by the Deutsche Forschungsgemeinschaft (DE 3578/3-1/Li 580/16-1, and SPP1839, SPP1840, SPP2196, GRK1885, SFB1372) is gratefully acknowledged. C.C. acknowledges additional funding from the German Federal Ministry of Education and Research (Professorinnenprogramm III). D.R.C. acknowledges funding from the European Union’s Horizon 2020 research and innovation program under the Marie Skłodowska-Curie grant agreement No. 893194. Computational resources for the simulations were provided by the HPC cluster CARL of the Carl von Ossietzky University Oldenburg funded by the DFG (Project No. INST 184/157-1 FUGG) and by the MWK.

Author contributions

A.D.S., C.L., D.C., and F.J. initiated this project. Y.R., D.R.C., S.A., and D.C. synthesized and characterized the crystals. X.T.N., D.T., K.W., and A.D.S. performed the experiments. A.D.S., X.T.N., C.L., D.T., and K.W. analyzed the data. A.D.S., C.C., M.S.R., M.L., and F.J. performed the calculations. A.D.S. wrote the manuscript draft with contributions from C.L., C.C., and D.C. All authors discussed the results and contributed to finalizing the manuscript.

Funding

Open Access funding enabled and organized by Projekt DEAL.

Competing interests

The authors declare no competing interests.

Additional information

Supplementary information The online version contains supplementary material available at <https://doi.org/10.1038/s41467-023-36654-2>.

Correspondence and requests for materials should be addressed to Antonietta De Sio.

Peer review information *Nature Communications* thanks Tushar Deb-nath and the other, anonymous, reviewer(s) for their contribution to the peer review of this work.

Reprints and permissions information is available at <http://www.nature.com/reprints>

Publisher’s note Springer Nature remains neutral with regard to jurisdictional claims in published maps and institutional affiliations.

Open Access This article is licensed under a Creative Commons Attribution 4.0 International License, which permits use, sharing, adaptation, distribution and reproduction in any medium or format, as long as you give appropriate credit to the original author(s) and the source, provide a link to the Creative Commons license, and indicate if changes were made. The images or other third party material in this article are included in the article’s Creative Commons license, unless indicated otherwise in a credit line to the material. If material is not included in the article’s Creative Commons license and your intended use is not permitted by statutory regulation or exceeds the permitted use, you will need to obtain permission directly from the copyright holder. To view a copy of this license, visit <http://creativecommons.org/licenses/by/4.0/>.

© The Author(s) 2023